Resonant X-Ray Scattering and Absorption for the Global and Local Structures of Cu-modified Metallothioneins in Solution

Meiyi Li,[†] Yu-Shan Huang,[‡] U-Ser Jeng,[‡*] I-Jui Hsu,[§*] YewChung Sermon Wu,[†*] Ying-Huang Lai,[¶] Chiu-Hun Su,[‡] Jyh-Fu Lee,[‡] Yu Wang,[‖] and Chia-Ching Chang[††‡‡]

[†]Department of Materials Science and Engineering, National Chiao Tung University, Hsinchu, Taiwan; [‡]National Synchrotron Radiation Research Center, Hsinchu, Taiwan; [§]Department of Molecular Science and Engineering, National Taipei University of Technology, Taipei, Taiwan; [¶]Department of Chemistry, Tunghai University, Taichung, Taiwan; [‖]Department of Chemistry, National Taiwan University, Taipei, Taiwan; [††]Department of Biological Sciences and Technology, National Chiao Tung University, Hsinchu, Taiwan; and [‡‡]Institute of Physics, Academia Sinica, Taipei, Taiwan

ABSTRACT With Cd and Zn metal ions removed from the native rabbit-liver metallothionein upon unfolding, Cu-modified metallothioneins (Cu-MTs) were obtained during refolding in solutions containing Cu^{I} or Cu^{II} ions. X-ray absorption near-edge spectroscopic results confirm the respectively assigned oxidation states of the copper ions in Cu^{I}-MT and Cu^{II}-MT. Global and local structures of the Cu-MTs were subsequently characterized by anomalous small-angle x-ray scattering (ASAXS) and extended x-ray absorption fine structure. Energy-dependent ASAXS results indicate that the morphology of Cu^{II}-MT resembles that of the native MT, whereas Cu^{I}-MT forms oligomers with a higher copper content. Both dummy-residue simulation and model-shape fitting of the ASAXS data reveal consistently rodlike morphology for Cu^{II}-MT. Clearly identified Cu-S, Cu-O, and Cu-Cu contributions in the extended x-ray absorption fine structure analysis indicate that both Cu^{I} and Cu^{II} ions are bonded with O and S atoms of nearby amino acids in a four-coordination environment, forming metal clusters smaller than metal thiolate clusters in the native MT. It is demonstrated that a combination of resonant x-ray scattering and x-ray absorption can be particularly useful in revealing complementary global and local structures of metalloproteins due to the atom specific characteristics of the two techniques.

INTRODUCTION

Metallothioneins (MTs) are small metalloproteins (~6–7 kDa) with rich cysteines that can accommodate a wide range of metal ions, such as Cd^{II}, Zn^{II}, Cu^{I}, and Ag^{I}, either within a single domain, as in the cases of yeast and fungus MTs, or within two domains, as with mammalian and crustacean MTs (1–6). The intriguing metal affinity of MTs is closely related to their biological functions, such as detoxification of metals and scavenging of reactive oxygen species, and their environmental applications, such as metal-pollution biomarkers (1,6). In general, MTs are classified (1) into three groups according to the sequence similarity; modification of MTs can also be achieved via in vivo (7) or in vitro (8) chemical/physical processes, with the native metal ions replaced by specific ones. In particular, successful replacement of metal ions via protein unfolding-refolding has further broadened the range of metal ions that can be encaptured in MTs (9,10). Among all metal-replaced MTs, Cu- and Mn-modified MTs are believed to play important roles in a variety of applications (1–6), especially molecular sensing (9,10).

As elucidated by the related crystal structures (11,12), there generally exist in MTs characteristic domains with metal clusters bonded to cysteinyl sulfur atoms. Details of the metal thiolate clusters of MTs have been studied by means of various spectroscopic techniques, such as ultraviolet (UV) optical absorption (2–6), NMR (11,13), and/or x-ray absorption spectroscopy (XAS) (14–19). For the rabbit liver MT, NMR and x-ray crystallographic results indicated structural features of two metal-containing domains (designated α and β) (14). Based on molecular dynamics simulation, Chan et al. (19) suggested that these two domains could be connected by a flexible chain for a dumb-bell-like shape in solution. Such extended morphology is reminiscent of the two-domain structure in *Triticum durum* metallothionein (1), but differs drastically from the globular case of *Saccharomyces cerevisiae* metallothionein, which contains only a single metal cluster (20).

During the past decade, the application of small-angle x-ray scattering (SAXS) to protein solutions has drawn considerable attention, due partly to advances in the related data-analysis algorithm (21,22) that allow structural models of proteins to be built on the basis of x-ray solution scattering data. More recently, combinations of SAXS with NMR, x-ray crystallography, and local structural characterization techniques such as XAS, optical absorption, or circular dichroism (CD), have provided further structural details of proteins in the solution state (17,18,23,24). Here, we report results from a combination of resonant x-ray absorption and anomalous small-angle x-ray scattering (ASAXS) studies of MTs in terms of supplementary global/local structural features, including the protein envelope, metal coordination geometry, and metal content. The technique of ASAXS is highly useful for determining the metal composition/distribution in complex systems such as core-shell

Submitted November 11, 2008, and accepted for publication May 1, 2009.

*Correspondence: usjeng@nsrrc.org.tw; ijuihsu@ntut.edu.tw or sermonwu@faculty.nctu.edu.tw

Editor: Kathleen B. Hall.

0006-3495/09/07/0609/9 $2.00

doi: 10.1016/j.bpj.2009.05.004

quantum dots (25), lipid-metal composites (26), and protein-metal complexes (27,28). However, application of ASAXS to MTs is very rarely reported, because the contribution to SAXS from the metal atoms is limited with respect to the contribution from the whole protein. To better correlate with ASAXS, parallel XAS measurements were made under the same sample conditions. Note, however, that XAS for protein solutions at ambient temperatures suffers severe effects from radiation damage and thermal fluctuations, and is much less often reported (29) compared to the case of smaller molecular compounds/complexes (30) or proteins at a low temperature of ~80 K (6,15–18). We have therefore taken particular caution by using a low-flux beam (with the penalty of long exposure time, of course).

By integrating the investigations of ASAXS and XAS at the Cu K-edge, we demonstrate that it is possible to obtain not only the size, shape, and copper content but also the oxidation state and the coordination geometries around the metal ions of the Cu-MTs, which are modified from the rabbit liver MT via a designated unfolding-refolding process. The obtained global and local structures of the Cu-modified MT provide an insight into variables that control the protein conformation and metal content. The result is crucial to developing an efficient unfolding-refolding procedure for modified MTs of specific metal content and stable morphology. One of the potential applications relates to the use of Cu-modified MT for a possible switch or sensor in a nano-device, based on the responses of the Cu-modified MT to an applied voltage: protected by protein from environmental fluctuations, Cu ions could be reduced or oxidized by accepting or releasing electrons upon change of electric potential in a device. In such an application, copper is preferred over other metal ions due to its high electrical conductivity.

MATERIALS AND METHODS

Materials and sample preparation

The Cd/Zn-metallothionein taken from rabbit livers (molecular mass 6012 Da; metal atoms excluded) was purchased from Sigma Aldrich (St. Louis, MO). The SDS-PAGE result of the native MT, with the cysteines modified by monobromobimane (mBrB), exhibited a single band, indicating that the native MT was of low polydispersity in molecular mass. Following the procedures detailed in previous reports (9,10), Cd and Zn ions of the protein were removed (apo-MT) in a solution containing 4.5 M urea, 10 mM Tris base (*tris*(hydroxymethyl)aminomethane), 0.1 M β-mercaptoethanol (β-ME), 0.2% mannitol (hexane-1,2,3,4,5,6-hexol), and 0.1 mM Pefabloc (4-(2-aminoethyl)benzenesulfonyl fluoride). The unfolded apo-MT was furthermore refolded in a series of Tris-base buffer solutions with $Cu(NO_3)_2$ or CuCl (Table 1) to obtain folded Cu^{II}-MT or Cu^{I}-MT. Circular dichroism (CD) data in the range 190–250 nm suggested that the secondary structures of both refolded Cu^{I}-MT and Cu^{II}-MT should be similar to that of the native MT, i.e., dominated by coils and turns. Ultraviolet (UV) absorption spectra, normalized to protein concentration, were measured for the apo-MT, Cu^{I}-MT, and Cu^{II}-MT solutions with 0.1 mM Tris base, using a Jasco spectrophotometer (model V-550 series, Tokyo, Japan); the protein concentration of each sample solution with 0.1 M HCl was calibrated by the electronic absorption of the peptide backbones of the apo-MT at 220 nm (ε_{220} = 48,000 M^{-1} cm^{-1} or 4.7 mg^{-1} mL cm^{-1}) (31). UV absorption spectra of both Cu^{I}-MT and Cu^{II}-MT manifested the characteristic ligand-to-metal charge transfer band of the M-S (cysteinyl sulfur) bond in the range 220–350 nm, especially the characteristic absorption shoulder at ~260 nm of copper ions (3,6). (Note that there is no aromatic amino acid in the MT that can contribute to any absorption in this region.) For comparison, there was no discernible absorption related to metal ions in this region for the apo-MT, assuring a complete removal of the native metal ions.

TABLE 1 Tris-base buffer solutions used for MT refolding

Solution no.	Urea	β-ME	Mannitol	Pefabloc	$Cu(NO_3)_2$ or CuCl + 10 mM ascorbic acid
1	2 M	0.1 mM	0.2%	0.1 mM	0.1mM
2	1 M	0.1 mM	0.2%	0.1 mM	0.1mM
3	0	0.1 mM	0.2%	0.1 mM	0.1mM
4	0	0.1 mM	0.2%	0.1 mM	0.5mM
5	0	0.1 mM	0%	0.1 mM	0.5mM
6	0	0.1 mM	0%	0.1 mM	0

Solutions are numbered 1 through 6. Buffer solution 6 was also used to prepare the sample solutions for ASAXS and XAS.

ASAXS measurement and data analysis

Native and Cu-modified MTs in Tris-base buffer solutions (2.5–10 mg/mL) were prepared for ASAXS measurements performed at the beamline 17B3 of the National Synchrotron Radiation Research Center (NSRRC) (32). Sample solutions were respectively sealed in 2-mm (x-ray path length) cells and measured at 283 K. To minimize radiation damages, the sample solution cell with large Kapton windows (5 mm in diameter) was gently rocked within an area 2 × 2 mm^2 to avoid prolonged spot (~0.5-mm beam diameter) exposure. Under x-ray energies near the Cu K-edge (8.979 keV) or off-resonant (10.5 keV), the ASAXS profiles collected at different time intervals (in the order of 10^2 s) overlapped well with one another, indicating that the protein morphology was insensitive to the radiation exposure during the measurement. As there was no observable Cu fluorescence interfering with the SAXS intensity at 10.5 keV, this beam energy was adopted as a reference in the ASAXS data analysis. One-dimensional ASAXS profiles were circularly averaged from the 2D patterns obtained using a MAR165 CCD detector. The scattering wavevector, $Q = 4\pi\lambda^{-1}\sin\theta$, defined by the scattering angle 2θ and wavelength λ, was calibrated by the diffraction peaks of silver behenate; for each x-ray energy adopted, the scattering intensity $I(Q)$ was recast into absolute intensity units using a polyethylene standard (25). To differentiate small variations in the ASAXS profiles, effects from detector noise, background scattering, incoming flux, and sample transmission were all rigorously corrected (32). The SAXS profiles of the native, Cu^{I}-modified, and Cu^{II}-modified MTs were concentration-independent, suggesting that these proteins were stable in morphology within the selected concentration range.

SAXS intensity distribution for monodisperse proteins in solution was modeled as $I(Q) = I_oP(Q)S(Q)$, with normalized form factor $P(Q)$ and structure factor $S(Q)$ (33–36). For dilute protein solutions with few interparticle interactions, $S(Q)$ is close to unity (33). Due to the presence of metal atoms in the MTs, the zero-angle scattering intensity,

$$I_o(E) = N_oC|f(E) - \rho_sV|^2, \quad (1)$$

may depend on the x-ray energy E (25–28). Here, N_o, C, ρ_s, and V denote, respectively, the aggregation number, protein concentration, scattering-length density of the solvent, and volume of the MT. Note that the concentration-normalized intensity, I_o/C, is linearly proportional to N_o (34,35). The scattering length, $f(E)$, is contributed by scattering length f_o summed over all the (energy-insensitive) nonmetal atoms and scattering length $f_m(E) = f_{mo} + f_m'(E) + if_m''(E)$ of the metal atom (25–28,37,38). The ratio $R(E)$ of two I_o values measured at an off-resonant energy E_{ref} and a near-resonant energy E can be expressed as

$$R(E) = |f_E - \rho_s V|^2 / |f_{E_{ref}} - \rho_s V|^2 = \left(f_r^2 + M^2 f_m''^2\right)_E / \left(f_r^2 + M^2 f_m''^2\right)_{E_{ref}}, \quad (2)$$

where $f_r(E) = f_o + M(f_{mo} + f_m'(E)) - \rho_s V$. As the incident beam energy approaches an absorption edge of the metal atom, $R(E)$ decreases significantly, allowing for the evaluation of metal content, M, using Eq. 2.

The SAXS data were first qualitatively examined for rodlike features under the Kratky-Porod approximation (35). This was then followed by quantitative fitting to the orientation-averaged form factor

$$\tilde{P}(Q) = \int_0^1 \left| \frac{2J_1(v)}{v} \frac{\sin(w)}{w} \right|^2 d\mu, \quad (3)$$

for rods of radius r and length L, where J_1 is the first-order Bessel function (33), $v = Qr(1-\mu^2)^{1/2}$, and $w = (1/2)QL\mu$. As a consistency check, the radius of gyration, $R_g = (r^2/2 + L^2/12)^{1/2}$, of the rods was calculated from the fitted r and L values and compared with the R_g value extracted from the model-independent Guinier approximation (33,39). The dummy-residue simulation package, developed by the Eurpean Molecular Biology Laboratory's Biological Small Angle Scattering Group, was adopted to give detailed protein envelopes (21,22).

X-ray absorption measurement and data analysis

X-ray absorption measurements for the MT solutions were made at the wiggler beamline BL-17C1 at the NSRRC. The beam was monochromatized with a double-crystal monochromator of Si(111) for energy resolution $\Delta E/E \approx 2 \times 10^{-4}$. The sample was sealed in a 1-mm cell with Kapton windows and measured at ~283 K for an alignment of the sample condition with that of ASAXS. Absorption spectra were taken in fluorescence mode with a 13-element solid-state detector in the energy range 8780–9880 eV. The first inflection point at 8979.0 eV of the absorption spectrum of a Cu foil was used for energy calibration. Previously, a slightly higher value of 8980.3 eV was used by Kau et al. (17). To minimize possible sample radiation damage in x-ray absorption measurements, the strategy was adopted of using a low flux beam with long exposure time, which greatly lengthened the overall data collection time up to 48 h for each complete spectrum accumulated over ~20 energy scans. Reproducible x-ray absorption near-edge spectroscopic (XANES) spectra for all scans under this data collection strategy indicated that radiation damage to the protein structure was negligible. The XAS data were corrected for background and normalized according to $\chi(k) = (\mu(k) - \mu_0(k))/\Delta\mu_0(0)$ by the AUTOBK program (40), with $\mu(k)$ the measured absorption coefficient, $\mu_0(k)$ the background, and $\Delta\mu_0(0)$ the edge jump. The wavenumber is defined as $k = (2m(E-E_0)/\hbar)^{1/2}$, where E is the photon energy, E_0 the threshold energy, $\hbar$ the Planck constant, and m the electron mass. Based on local maxima of the first-derivative profiles of the XANES spectra, $d\mu/dE$, E_0 was set at 8990.4 eV and 8989.8 eV for Cu^{I}-MT and Cu^{II}-MT, respectively. The $\chi(k)$ in the EXAFS region $2.6 \le k \le 12.6$ Å^{-1} was further weighted by k^3 and then Fourier-transformed into the R-space as FT($k^3\chi(k)$). The EXAFS data analysis was done according to

$$\chi(k) = S_0^2 \sum_j \frac{N_j(k)F_j(k)}{kR_j^2} \sin\left[2kR_j + \delta_j(k)\right] e^{-\frac{2R_j}{\lambda}} e^{-2k^2\sigma_j^2}, \quad (4)$$

based on plane wave single scattering (41), where $F_j(k)$ is the backscattering amplitude from each of the N_j atoms in the shell at distance R_j (relative to the absorbing atom), $\exp(-2k^2\sigma_j^2)$ the Debye-Waller factor with the mean-squared displacement σ_j^2, S_0 the amplitude reduction factor, $\delta_j(k)$ the total phase shift, and $\lambda(k)$ the photoelectron mean free path. With S_0 fixed at unity and the values of $F_j(k)$, $\delta_j(k)$, and $\lambda(k)$ calculated using a curved-wave ab initio procedure in the FEFF7 code (42), we fitted FT($k^3\chi(k)$) in the range $1.7 \le R \le 4.0$ Å with the fitting parameters ΔE_0 (small variation in E_0), R_j, σ_j^2, and N_j, using a nonlinear least-square fitting algorithm implemented by FEFFIT program (40). In the fitting algorithm, ΔE_0 was confined as a common fitting parameter for all scattering paths. Data fitting quality was evaluated with the goodness-of-fit factor, defined as

$$R_{fit} = \frac{\sum_{i=1}^{n} \left\{ [\mathrm{Re}(f_i)]^2 + [\mathrm{Im}(f_i)]^2 \right\}}{\sum_{i=1}^{n} \left\{ [\mathrm{Re}(\tilde{\chi}_{\mathrm{data}\ i})]^2 + [\mathrm{Im}(\tilde{\chi}_{\mathrm{data}\ i})]^2 \right\}}, \quad (5)$$

where $\tilde{\chi} = k^3\chi$ and n is the number of evaluations of f_i, with $f_i = \tilde{\chi}_{\mathrm{data}\ i} - \tilde{\chi}_{\mathrm{model}\ i}$ (and hence R_{fit}) minimized in the nonlinear least-square fitting algorithm (40,41).

RESULTS AND DISCUSSION

Native MT, unfolded apo-MT, and refolded apo-MT

SAXS data measured for the native MT, the unfolded apo-MT, and the refolded apo-MT, are displayed in Fig. 1. With the Kratky-Porod approximation, SAXS of the native MT (10 mg/mL) reveals a rodlike feature; the data are therefore fitted (*dashed curve*) using the rodlike model with rod length $L = 74 \pm 2$ Å and rod radius $r = 12.7 \pm 0.3$ Å. The R_g value (23.4 ± 0.4 Å) deduced from L and r is consistent with that obtained from the Guinier approximation (24 ± 2 Å) (Fig. 1 *a*, *inset*). Using the measured absolute intensity, $I(0)$, and the calculated scattering length density of the protein (34,35), 14.0×10^{-6} Å^{-2} (corresponding to an electron density of 0.50 e^-/Å^3), the aggregation number of the MT is estimated from Eq. 1 to be $N_o \approx 1$, i.e., the molecular mass scaled from I_o is ~6.8 kDa (43). Thus, the large R_g value is believed to be contributed mainly by the extended rodlike morphology of 62 amino acids (AA) of the MT, rather than by protein aggregation. Furthermore, the rodlike shape and R_g value are consistent with the result from dummy-residue simulation shown in Fig. 1 *b*, where the simulated protein envelope is extended and dumbbell-like, with metal clusters situated at both ends and $R_g = 24.8 \pm 0.4$ Å. A large R_g value with small molecular mass is common for rodlike proteins such as the light harvesting protein (PDB code 1DX7, 48 AA, $R_g = 22$ Å). In contrast, globular MTs with a similar molecular mass tend to have lower R_g values. For instance, $R_g = 10$ Å for *Saccharomyces cerevisiae*, which has a single metal cluster domain (PBD code 1AQR, 40 AA).

For the unfolded apo-MT, SAXS data manifest a power-law scattering feature $I(Q) \propto Q^{-1}$ in the higher-Q region (Fig. 1), which implies a collapse of the tertiary structure of the metal-depleted protein. For comparison, $I(Q) \propto Q^{-2}$ corresponds to random coils of a Gaussian chain conformation (39). On the other hand, the SAXS profile of the refolded apo-MT differs significantly from that of the native MT, particularly in the low-Q region, which indicates that the apo-MT cannot correctly refold to the same morphology of the native MT; instead, apo-MT forms oligomers in the buffer solution with no metal ions. Correspondingly, the

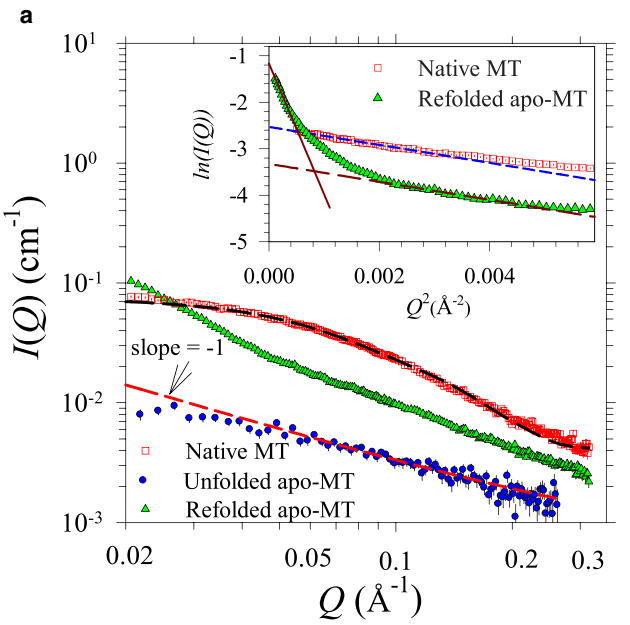

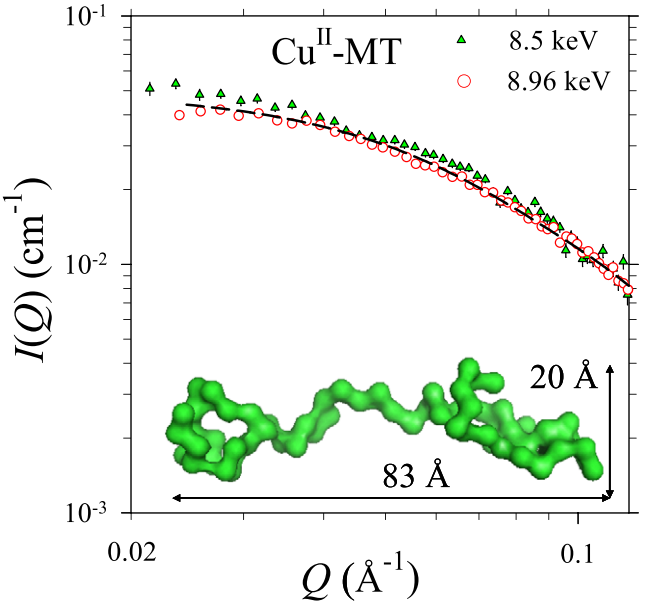

FIGURE 2 ASAXS data of the Cu^{II}-MT measured at 8.5 keV (E_{ref}) and 8.960 keV (fitted with the dashed curve for a rod shape). (*Inset*) Corresponding protein envelope obtained with the dummy-residue simulation.

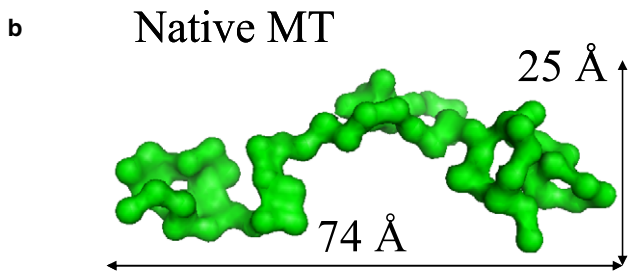

FIGURE 1 (*a*) SAXS data of the native MT (10 mg/ml) and unfolded apo-MT (2.5 mg/ml) are fitted with a rodlike shape (*upper dashed curve*) and power-law scattering $I(Q) \propto Q^{-1}$ (*lower dashed line*), respectively. Also shown are the SAXS data of the refolded apo-MT (10 mg/ml). All data were collected with 10.5-keV x-rays. (*Inset*) Guinier approximations (*dashed lines*) for the SAXS data of the native MT and refolded apo-MT (*solid* and *long-dashed lines* indicate the higher- and lower-bound R_g values). (*b*) Protein envelope of the native MT obtained from the dummy-residue simulation with the SAXS data.

Guinier approximation using the SAXS data of the apo-MT reveals polydisperse R_g values ranging from 24 Å for the monomers to 90 Å for the oligomers (Fig. 1, *inset*).

Resonant x-ray scattering of Cu-MTs

ASAXS profiles of the Cu^{II}-MT measured at two different x-ray energies are shown in Fig. 2. In contrast to the apo-MT refolding in the absence of metal ions, the resemblance between these two ASAXS profiles and that of the native MT indicates that apo-MT can refold into a shape similar to that of native MT in the presence of Cu^{II} ions. Using the form factor of rods, we can adequately fit the SAXS data of the Cu^{II}-MT taken at 8.960 keV with $L = 83 \pm 2$ Å and $r = 10 \pm 2$ Å (Fig. 2); the corresponding R_g value extracted from the L and r values is 25 ± 2 Å, the same as that obtained from the Guinier approximation. These structural parameters are also consistent with the R_g value (26 Å) and the elongated protein envelope obtained using the dummy-residue simulation (Fig. 2 *inset*, with $2r$). Furthermore, the ASAXS profile obtained with 8.960 keV (close to the Cu K-edge absorption) is lower in intensity than that obtained with 8.5 keV due to the presence of copper atoms in the Cu^{II}-MT. Based on Eq. 2, an averaged copper content of $M = 4 \pm 2$ Cu^{II}/protein is derived from the intensity ratio, $R(E)$, of the ASAXS profile at $E = 8.5$ keV (the reference energy) to that at 8.960 keV (0.97). The large uncertainty of the M value is due to the measurement uncertainty, ± 0.01, of the R(E) value, based on the error propagation in Eq. 2. The copper content is marginally consistent with the inductively coupled plasma mass spectroscopy (ICP-MS) result of 1.8 ± 0.2 copper ions per Cu^{II}-MT. Compared to the more compact native MT composed of the metal thiolate clusters, the slightly extended morphology of the Cu^{II}-MT may be related to the insufficient number of metal ions (therefore, a different local coordination geometry). Indeed, XAS results detailed below do suggest dissimilar correlation between the copper ions in the Cu^{II}-MT and the metal thiolate clusters of the native MT (3,5,6,19).

Shown in Fig. 3 is the concentration-normalized SAXS profile of Cu^{I}-MT, which differs significantly from that of the native MT. The substantially larger I_o/C value compared to that of the native MT indicates that Cu^{I}-MT forms oligomers and cannot refold back to the native-MT morphology. Nevertheless, a mean R_g value of 40 ± 4 Å can still be extracted from the Guinier approximation (Fig. 3, *inset*), implying a small degree of polydispersity for the oligomers

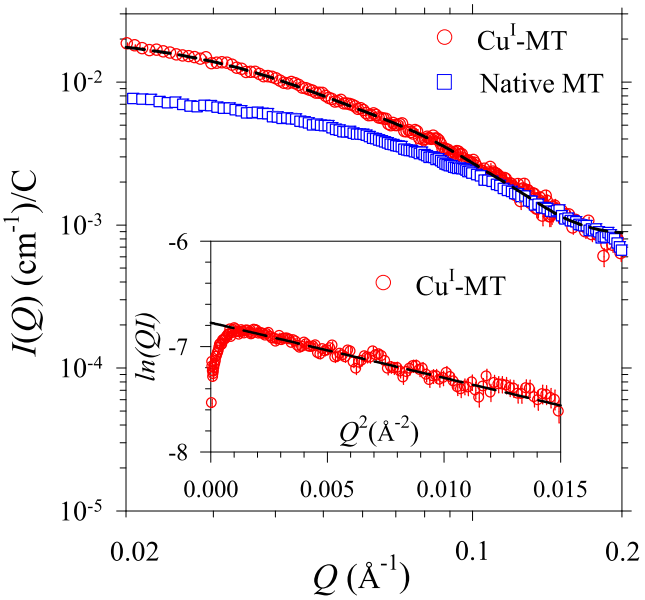

FIGURE 3 Concentration-normalized SAXS data (with 10.5 keV) of native MT (10 mg/ml) and Cu^{I}-MT (2.5mg/ml). Data of Cu^{II}-MT are fitted with a rod model (*dashed curve*). (*Inset*) The corresponding data fitted with the Kratky-Porod approximation (*dashed line*).

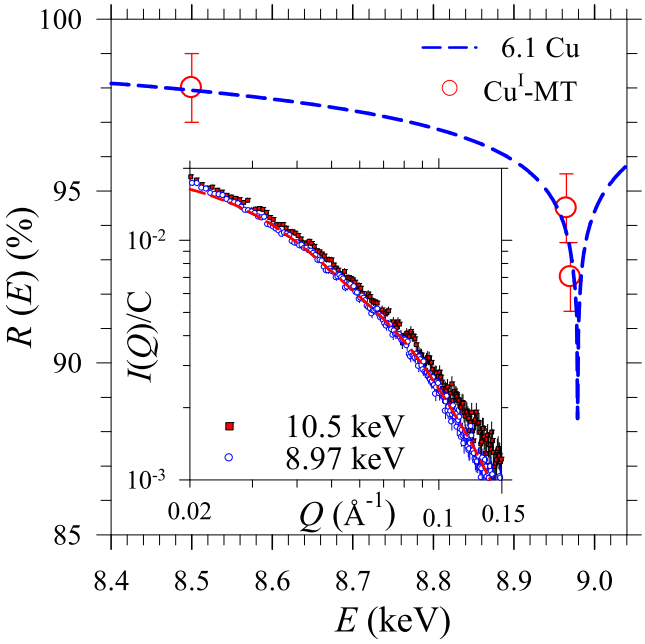

FIGURE 4 The $R(E)$ values of Cu^{I}-MT measured at 8.5, 8.965, and 8.970 keV, with $E_{ref} = 10.5$ keV, are fitted with 6.1 Cu (*dashed curve*) using Eq. 2. (*Inset*) ASAXS data measured at 10.5 and 8.970 keV. The 8.970 keV data are fitted with a rodlike model (*dashed curve*). For clarity, ASAXS data measured with 8.5- and 8.965-keV x-rays are not shown.

(likely dimers or trimers, as estimated from the measured I_o value). Furthermore, the Kratky-Porod approximation reveals a rodlike shape with an averaged rod radius of ~15 Å (as estimated from the slope of the fitted line in the inset of Fig. 3) for the Cu^{I}-MT oligomers (39). Using the rod form factor, we can adequately fit the SAXS data with $L = 132 \pm 5$ Å and $r = 18.9 \pm 1$ Å (Fig. 3). With a reference intensity measured at $E_{ref} = 10.5$ keV, the ASAXS intensity of the Cu^{I}-MT measured at 8.5, 8.965, and 8.970 keV decreases systematically to 98%, 95%, and 92%, respectively, as the x-ray energy approaches the Cu K-edge at 8.979 keV. These ASAXS intensity ratios, $R(E)$, clearly indicate a substantial amount of copper in the Cu^{I}-MT. Using Eq. 2 with a nonlinear least-square fitting process, we can fit these $R(E)$ ratios reasonably well with $M = 6.1 \pm 0.9$ Cu ions/Cu^{I}-MT (Fig. 4), which is close to the value 7.7 ± 0.2 Cu ions obtained from ICP-MS.

X-Ray absorption of Cu-MTs

The XANES studies on Cu-modified MTs at the Cu K-edge, shown in Fig. 5. reveal the local structure of the copper ions. Based on the first derivative, $d\mu/dE$, of the spectrum (Fig. 5, *inset*) of Cu^{II}-MT, the single main peak at 8985.9 eV before the edge at 8997 eV is assigned to the $1s \rightarrow 4p$ transition in Cu^{II} complexes, whereas the first derivative of the Cu^{I}-MT spectrum exhibits two characteristic peaks at 8981.8 eV (44) and 8985.4 eV, implying that Cu^{I} in Cu^{I}-MT has a covalent bonding character in the Cu-ligand bond (17,44) stronger than that found in normal Cu^{I} complexes. The XANES results clearly indicate that the average oxidation states of Cu^{I}-MT and Cu^{II}-MT are Cu^{I} and Cu^{II}, respectively. In a previous investigation by Meloni et al. (3) on the metal ion exchange of Zn_7MT-3 with Cu^{II} ions, Cu^{II} ions were found to be reduced to Cu^{I} before replacing Zn^{II} ions in the native MT, probably due to the higher affinity of Cu^{I}, compared to Zn^{II}, for forming metal thiolate clusters in the

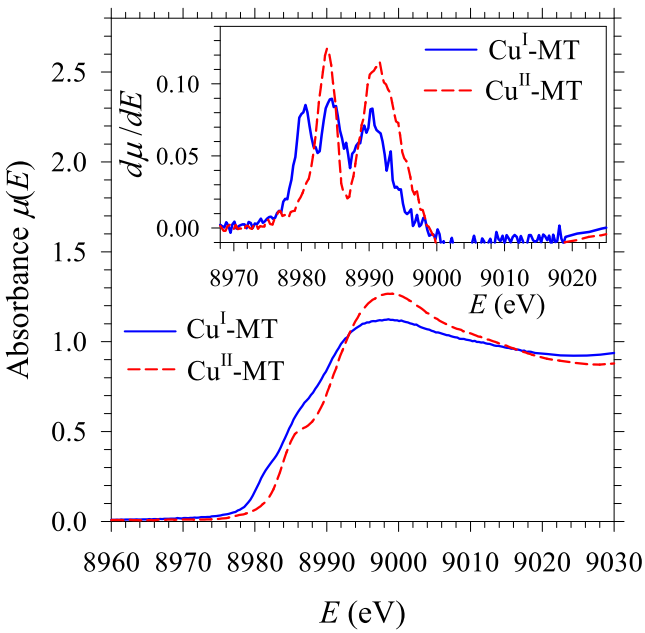

FIGURE 5 XANES data of Cu^{I}-MT and Cu^{II}-MT. (*Inset*) The corresponding $d\mu/dE$ profiles.

MT; in that reaction, it was proposed that thiolate ligands were oxidized to disulfides concomitantly with Zn^{II} release. In contrast, by taking the unfolding-refolding route as an alternative, in which the native thiolate clusters were removed from the MT in the unfolding before the introduction of Cu^{II} ions into the solution, the observations presented here indicate that Cu^{II} ions can indeed be incorporated into the apo-MT during the subsequent refolding without being reduced to Cu^{I}.

Guided by the XANES results and the structural information from the Cambridge Crystallographic Data Center (CCDC) (45) on four- and five-coordinate Cu complexes (16,17,44), we furthermore fit the EXAFS data of the two Cu-modified MTs. The best fitted results are displayed in Fig. 6, *a* and *b*, with the fitted $k^3\chi(k)$ spectra shown as insets and the corresponding parameters summarized in Table 2. Two possible models based on the fitting results are depicted in Fig. 7, *a* and *b*. In the case of Cu^{I}-MT, the fitted parameters imply that Cu^{I} is mainly coordinated by four ligands of Cu-O/N and Cu-S(Cys) bonds, with average distances of 1.96(1) Å and 2.49(3) Å, respectively. The Cu-O/N bonding is attributed to O/N atoms of nearby amino acids. It is likely, furthermore, that some of the oxygen atoms belonging to carbonyl groups (C=O) of the amino acids may act as linkers for Cu ions, which gives the observed Cu-Cu distance of 3.35(1) Å and a bond angle ∠Cu-O-Cu of 117°. Consequent associated backscattering from the C atoms of the amino acids, at a distance of 2.79(5) Å, can be derived. Based on the average distance, 1.23 Å, of the C=O (46), the corresponding bond angle of ∠Cu-O-C is estimated to be ~121°.

As indicated in Table 2, a Cu-Cu distance of 3.80(1) Å (Cu clustering) also exists in Cu^{I}-MT. Such long-range interactions may be rationalized by an S(Cys) bridged ligand between two coppers with Cu-S bonds at a distance of 2.49(3) Å. A similar S(Cys) bridging case was observed previously in the Zn-based MT (PDB code 4MT2), which has two similar Zn-S distances of 2.48 Å and 2.37 Å, and a long Zn-Zn distance of 3.88 Å (11). In Table 2, a further-away S-backscattering at a distance of 3.05(2) Å was allocated, which might be contributed by unbonded S atoms of distant cysteine residues, as suggested by the intermolecular Cu-S distance of 2.89 Å found in the CUPHAU code of the CCDC (45). Based on the fitted parameters and the coordination chemistry described in detail above, a possible model for the local geometry of Cu^{I} in Cu^{I}-MT is given in Fig. 7 *a*. The model is characterized by three copper pairs interconnected via weak Cu-S(Cys) interactions in the protein; each Cu pair is composed of two C=O bridged Cu ions in a four-coordinate geometry.

On the other hand, the structural parameters detailed in Table 2 for Cu^{II}-MT indicate that each Cu^{II} ion is coordinated to two S and two O atoms at the two Cu-S(Cys) and Cu-O distances of 2.17(1) and 2.61(3) Å, respectively. As suggested by the codes of BIWBEP, GUGTIL, and URCOPS in CCDC (45), ligands of either protein-bound H_2O or amino acids (via carboxylate or bridge oxygen) may end up with the long Cu-O distance observed in Cu^{II}-MT. The C atom of the C-S bond in a cysteine is detected at a distance of 3.30(5) Å, which resembles the case of the MT protein of 4MT2, which has an average Zn-C distance of ~3.34 Å (11). The observed Cu backscattering at a distance of 3.71(2) Å can be treated as an S(Cys) bridged (i.e., Cu-S-Cu) case with a short Cu-S bond distance of 2.17(3) Å. Such a Cu-Cu distance is slightly shorter than the Zn-Zn distance (~3.88 Å) in 4MT2 and the Cu-Cu distance of 3.80(1) Å in Cu^{I}-MT; comparable M-M distances do exist in certain systems, for example, BAYBAE in the CCDC (45). We have incorporated all aspects of the coordinate geometry of Cu^{II} in Cu^{II}-MT described above into the model given in Fig. 7 *b*, which comprises a more compact tricopper cluster linked by Cu-S(Cys) bonds (as contrasted with the metal cluster in Cu^{I}-MT, cf. Fig. 7 *a*).

Based on the x-ray absorption results, both Cu^{I} and Cu^{II} ions can be incorporated into MT for the Cu^{I}-MT and Cu^{II}-MT via bonding with O and S atoms. The Cu clusters formed (three loosely interconnected copper pairs in Cu^{I}-MT and one tricopper cluster in Cu^{II}-MT (Fig. 7)), however, are characteristically different from the metal thiolate clusters of the native protein formed with five Cd and two Zn ions through S(Cys) bonding.

Correlations between local and global structures

With the global and local structures of Cu-MTs clarified, we may now address the possible mechanism during the unfolding-refolding process of the rabbit-liver apo-MT in the presence of Cu^{I} and Cu^{II}. The metal thiolate clusters of Cd^{II} and Zn^{II} (d^{10} electronic configuration) within the native MT are believed to have tetrahedral coordination geometry with

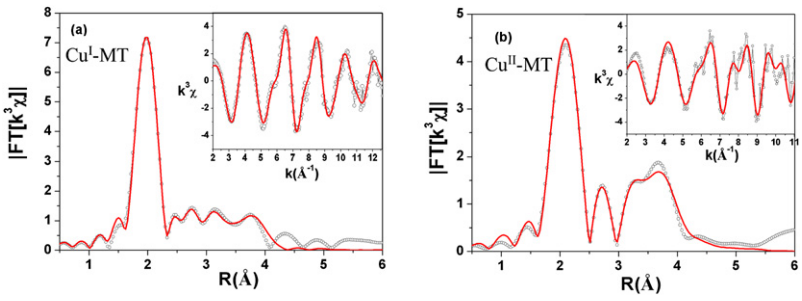

FIGURE 6 Fourier-transformed amplitudes, FT($k^3\chi(k)$) (*open circles*), of Cu^{I}-MT (*a*) and Cu^{II}-MT (*b*) are respectively fitted (*solid curves*) using the parameters summarized in Table 2. (*Insets*) The respectively fitted $k^3\chi(k)$ data.

TABLE 2 Parameters used in fitting the k^3-weighted EXAFS data of Cu^I-MT and Cu^{II}-MT

	Cu^I-MT			Cu^{II}-MT		
Bond type	N	R (Å)	σ^2 (Å^2)	N	R (Å)	σ^2 (Å^2)
Cu-O	3.5	1.96(1)	0.0045(2)	1.67	2.61(3)	0.008(3)
Cu-S	0.33	2.49(3)	0.007(3)	2	2.17(1)	0.0075(6)
Cu-C	1	2.79(5)	0.009(3)	2	3.30(5)	0.005(6)
Cu-S	1	3.05(2)	0.007(6)			
Cu-Cu	1	3.35(1)	0.008(1)			
Cu-Cu	1	3.80(1)	0.007(1)	1.33	3.71(2)	0.003(1)
Δk (Å^{-1})	[2.55, 12.55]			[2.75, 10.05]		
ΔR (Å)	[1.72, 3.99]			[1.72, 3.99]		
R_{fit}	0.2%			1.1%		
χ^2	21.69			19.95		
χ_v^2	4.87			4.38		

Parameters include the coordination number, N, the distance R relative to Cu, and the relative mean-square displacement, σ^2. Fitting ranges are indicated by Δk and ΔR, respectively. The fitting quality is evaluated by the goodness-of-fit factors R_{fit}, χ^2, and χ_v^2 ($\equiv \chi^2/v$), where v is the difference between the number of independent data points and the number of parameters used in the fitting.

metals bonded to four S atoms of Cys. To replace Cd^{II} and Zn^{II} in the native MT with Cu^I (d^{10}) or Cu^{II} (d^9), both changes in charge distribution and chemical bonding between metal ions and amino acids have to be taken into account. During the refolding process of the apo-MT in the presence of Cu^I, the difference in charge between the metal ions is expected to perturb the refolding of the MT, despite the fact that Cu^I has the same d^{10} electronic configuration for forming metal thiolate clusters; the extra charge after forming the Cu^I-bound MT may be dissipated to nearby amino acids via the formation of disulfide bonds, as suggested in a previous study (3). Specifically, each of the native metal ions (Cd^{II} or Zn^{II}) in MT is bound to four S(Cys) ligands, whereas there is less than one Cys on average in Cu^I-MT for each pair of Cu^I. Nonbonded S(Cys) ligands of neighboring Cu^I-MT may thus attract each other via disulfide interactions in the refolding process, leading to the formation of oligomers (as observed by ASAXS). On the other hand, during refolding with Cu^{II} ions, there is no charge difference from the native Cd^{II} and Zn^{II}; thus, Cu^{II}-MT can easily refold to a shape similar to that of the native MT. Nevertheless, with one less d orbital electron (d^9), the tetrahedral geometry may not be stable due to the Jahn-Teller distortion, and part of the Cu^{II} ions may then be dissociated into the dialysis solution (i.e., solution 6 in Table 1) during the last step of the refolding.

In general, the two types of copper clusters extracted from the XAS results for the two Cu-MTs conform, approximately, to their respective global morphologies revealed by SAXS. The extended rodlike morphology of Cu^I-MT oligomers corresponds to a more open local structure with three loosely connected copper pairs, whereas the better-refolded morphology of Cu^{II}-MT comprises a more compact tricopper cluster. With a metal content (six to seven Cu) comparable to that of the native MT (five Cd and two Zn), however, Cu^I-MT could only form oligmers; morphologically similar to the native MT, Cu^{II}-MT incorporated a lower metal content of four Cu ions. It hence appears that Zn^{II} ions (with the correct +2 charge and d^{10} electronic configuration) can be more suitable than Cu^I or Cu^{II} ions in such unfolding-refolding MT modification, provided of course that electrical conductivity of the modified MT is not a major concern in subsequent applications.

Meloni et al. (3) recently established an empirical relation between the UV absorption of a Cu-replaced Zn_7-MT (mainly the absorption at 262 nm) and the Cu content of the protein. Combining all ASAXS, XAS, ICP-MS, and UV absorption results for the two Cu-MTs, we may reach a similar conclusion, that UV absorption of the protein in the region of 220–350 nm is closely related to the copper content. Nevertheless, complications arise in quantitatively correlation of Cu-S interactions with UV absorption, as local environments

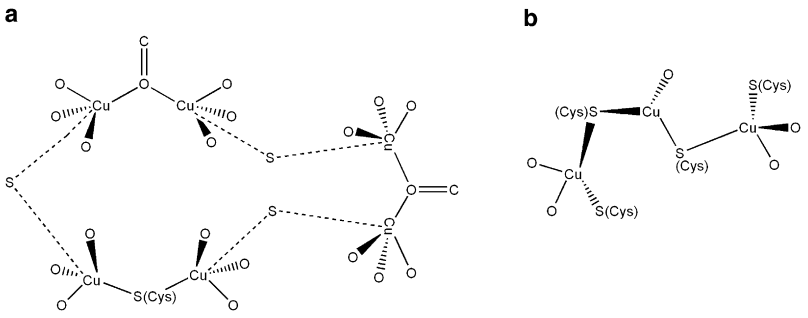

FIGURE 7 Possible models for the local geometries of Cu^I in Cu^I-MT (*a*) and Cu^{II} in Cu^{II}-MT (*b*).

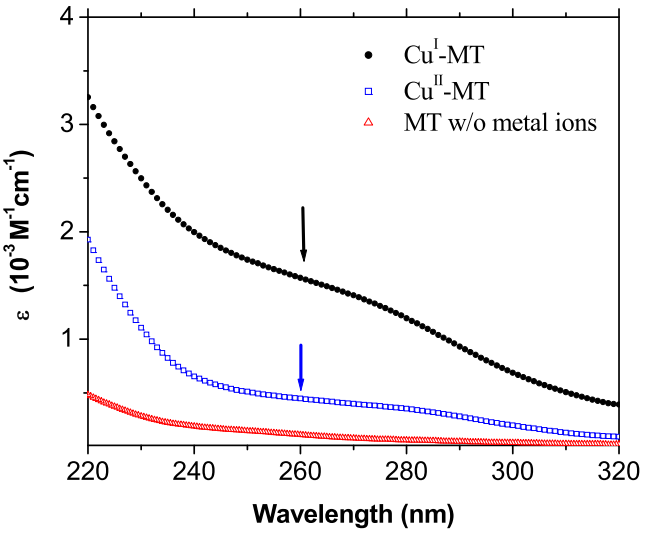

FIGURE 8 UV absorption spectra (ε) of Cu^{I}-MT, Cu^{II}-MT, and apo-MT (without metal ions). Arrows mark the characteristic absorption shoulder (~262 nm) of the binding of copper ions with the S atoms of cysteines.

and Cu-S interactions in the two Cu-MTs are likely very different. Specifically, the electronic configuration of Cu^{I} in Cu^{I}-MT is d^{10}; hence, Cu^{I} has only the sp^3 hybrid orbitals to overlap with the 3*p* orbitals of S in forming Cu-S bonding; in contrast, with the d^9 configuration, Cu^{II} in Cu^{II}-MT can use the unoccupied *d* orbital to form Cu-S bonds, leading to valence orbitals that differ from that in Cu^{I}-MT. In other words, the numbers (or their ratio) of Cu-S bonds in the two different types of Cu-MTs can be evaluated from the UV absorption spectra (Fig. 8) only when differences in the ligand valence orbitals of Cu^{I} and Cu^{II} are carefully accounted for.

CONCLUSIONS

We have demonstrated that resonant x-ray scattering (ASAXS) and x-ray absorption can be uniquely combined to provide direct global morphology and local coordination geometry of the metal ions for metallothioneins in solution. The size, rodlike morphology, and copper content of the modified Cu-MTs are revealed by ASAXS, whereas the coordination geometries around copper ions are elucidated by XAS as being in a four-coordinate mode bonded to O and S atoms of the amino acids and the small metal clusters. Global morphology and local metal ligand bonding of both Cu^{I}-MT and Cu^{II}-MT are found to deviate from the native MT, but to a different extent in each case. Overall, the integrated structural information gives insights into the mechanism of unfolding-refolding for the production of Cu-MTs from native ones. The same approach can be easily applied to other metalloproteins containing different metal ions due to the atom-specific character of x-ray resonance scattering and x-ray absorption.

We thank the National Nano Device Laboratories for the use of ICP-MS. Helpful discussions with Dr. H.-L. Chen are acknowledged, as are comments and proofreading by Dr. A. C. Su.

REFERENCES

1. Bilecen, K., U. H. Ozturk, A. D. Duru, T. Sutlu, M. V. Petoukhov, et al. 2005. *Triticum durum* metallothionein. *J. Biol. Chem.* 280:13701–13711.
2. Kägi, J. H. 1991. Overview of metallothionein. *Methods Enzymol.* 205:613–626.
3. Meloni, G., P. Faller, and M. Vašák. 2007. Redox silencing of copper in metal-linked neurodegenerative disorders. *J. Biol. Chem.* 282:16068–16078.
4. Funes, V., J. Alhama, J. K. Navas, J. Lopes-Barea, and J. Peinado. 2006. Ecotoxicological effects of metal pollution in two mollusk species from the Spanish South Atlantic littoral. *Environ. Pollut.* 139:214–223.
5. Roschitzki, B., and M. Vašák. 2002. A distinct Cu^4-thiolate cluster of human metallothionein-3 is located in the N-terminal domain. *J. Biol. Inorg. Chem.* 7:611–616.
6. Stillman, M. J. 1995. Metallothioneins. *Coord. Chem. Rev.* 144:461–511.
7. Tio, L., L. Villarreal, S. Atrian, and M. Capdevila. 2004. Functional differentiation in the mammalian metallothionein gene family. *J. Biol. Chem.* 279:24403–24413.
8. Suzuki, K. T., and T. Maitani. 1981. Metal-dependent properties of metallothionein. *Biochem. J.* 199:289–295.
9. Chang, C.-C., K.-W. Sun, S.-F. Lee, and L.-S. Kan. 2007. Self-assembled molecular magnets on patterned silicon substrates: bridging bio-molecules with nanoelectronics. *Biomaterials.* 28:1941–1947.
10. Liu, Y.-L., H.-T. Lee, C.-C. Chang, and L.-S. Kan. 2003. Reversible folding of cysteine-rich metallothionein by an overcritical reaction path. *Biochem. Biophys. Res. Commun.* 306:59–63.
11. Braun, W., M. Vašák, A. H. Robbins, C. D. Stout, G. Wagner, et al. 1992. Comparison of the NMR solution structure and the x-ray crystal structure of rat metallothionein-2. *Proc. Natl. Acad. Sci. USA.* 89:10124–10128.
12. Robbins, A. H., D. E. McRee, M. Williamson, S. A. Collett, N. H. Xuong, et al. 1991. Refined crystal structure of Cd, Zn metallothionein at 2.0 Å resolution. *J. Mol. Biol.* 221:1269–1293.
13. Otvos, J., and I. M. Armitage. 1980. Structure of the metal clusters in rabbit liver metallothionein. *Proc. Natl. Acad. Sci. USA.* 77:7094–7098.
14. Arcovito, A., M. Benfatto, M. Cianci, S. S. Hasnain, K. Nienhaus, et al. 2007. X-ray structure analysis of a metalloprotein with enhanced active-site resolution using in situ x-ray absorption near edge structure spectroscopy. *Proc. Natl. Acad. Sci. USA.* 104:6211–6216.
15. George, G. N., J. Byrd, and D. R. Winge. 1988. X-ray absorption studies of yeast copper metallothionein. *J. Biol. Chem.* 263:8199–8203.
16. Smith, T. A., K. Lerch, and K. O. Hodgson. 1986. Structural study of the copper sites in metallothionein from *Neurospora crassa*. *Inorg. Chem.* 25:4677–4680.
17. Kau, L. S., D. J. Spira-Solomon, J. E. Penner-Hahn, K. O. Hodgson, and E. I. Solomon. 1987. X-ray absorption edge determination of the oxidation state and coordination number of copper: application to the type 3 site in *Rhus vernicifera* laccase and its reaction with oxygen. *J. Am. Chem. Soc.* 109:6433–6442.
18. Bogumil, R., P. Faller, P. A. Binz, M. Vašák, J. M. Charnock, et al. 1998. Structural characterization of Cu^{I} and Zn^{II} sites in neuronal-growth inhibitory factor by extended X-ray absorption fine structure (EXAFS). *Eur. J. Biochem.* 255:172–177.
19. Chan, J., M. E. Merrifield, A. V. Soldatove, and M. J. Stillman. 2005. XAFS spectral analysis of the cadmium coordination geometry in cadmium thiolate clusters in metallothionein. *Inorg. Chem.* 44:4923–4933.
20. Sayers, Z., P. Brouillon, D. I. Svergun, P. Zielenkiewicz, and M. H. J. Koch. 1999. Biochemical and structural characterization of recombinant copper-metallothionein from *Saccharomyces cerevisiae*. *Eur. J. Biochem.* 62:858–865.
21. Svergun, D. I., M. V. Petoukhov, and M. H. J. Koch. 2001. Determination of domain structure of proteins from x-ray solution scattering. *Biophys. J.* 80:2946–2953.

22. Koch, M. H. J., P. Vachette, and D. I. Svergun. 2003. Small-angle scattering: a view on the properties, structures and structural changes of biological macromolecules in solution. *Q. Rev. Biophys.* 36:147–227.

23. Grishaev, A., J. Wu, J. Trewhella, and A. Bax. 2005. Refinement of multidomain protein structures by combination of solution small-angle x-ray scattering and NMR data. *J. Am. Chem. Soc.* 127:16621–16628.

24. Shiu, Y.-J., U. Jeng, Y.-S. Huang, Y.-H. Lai, H.-F. Lu, et al. 2008. Global and local structural changes of cytochrome *c* characterized by a multigroup unfolding process. *Biophys. J.* 94:4828–4836.

25. Sheu, H.-S., U. Jeng, W.-J. Shih, Y.-H. Lai, C.-H. Su, et al. 2008. Phase separation inside the CdTe CdSe type II quantum dots revealed by synchrotron x-ray diffraction and scattering. *J. Phys. Chem. C.* 112:9617–9622.

26. Bota, A., Z. Varga, and G. Goerigk. 2007. Biological systems as nanoreactors: anomalous small-angle scattering study of the CdS nanoparticle formation in multilamellar vesicles. *J. Phys. Chem. B.* 111:1911–1915.

27. Stuhrmann, H. B. 1980. Anomalous dispersion of small-angle scattering of horse-spleen ferritin at the iron *K* absorption edge. *Acta Crystallogr. A.* 36:996–1001.

28. Miake-Lye, R. C., S. Doniach, and K. O. Hodgson. 1983. Anomalous x-ray scattering from terbium-labeled parvalbumin in solution. *Biophys. J.* 41:287–292.

29. Hsu, I.-J., Y.-J. Shiu, U. Jeng, T.-H. Chen, Y.-S. Huang, et al. 2007. A solution study on the local and global structure changes of cytochrome *c* and lysozyme. *J. Phys. Chem. A.* 111:9286–9290.

30. Mahadevan, V., J. L. DuBois, B. Hedman, K. O. Hodgson, and T. D. P. Stack. 1999. Exogenous substrate reactivity with a $[Cu(III)_2O_2]^{2+}$ core: structural implications. *J. Am. Chem. Soc.* 121:5583–5584.

31. Vasák, M., J. H. R. Kägi, B. Holmquist, and B. L. Vallee. 1981. Spectral studies of cobalt (II)- and nickel (II)-metallothionein. *Biochemistry.* 20:6659–6664.

32. Lai, Y. H., Y. S. Sun, U. Jeng, J. M. Lin, T.-L. Lin, et al. 2006. An instrument for time-resolved and anomalous simultaneous small- and wide-angle x-ray scattering (SWAXS) at SRRC. *J. Appl. Cryst.* 39:871–877.

33. Chen, S. H. 1986. Small angle neutron scattering studies of the structure and interaction in micellar and microemulsion systems. *Annu. Rev. Phys. Chem.* 37:351–399.

34. Huang, Y. S., U. Jeng, Y.-J. Shiu, Y.-H. Lai, and Y.-S. Sun. 2007. SAXS-revealed charge interaction and temperature effects on the solution structure of lysozyme. *J. Appl. Cryst.* 40:s165–s169.

35. Lin, T.-L., U. Jeng, C.-S. Tsao, W.-J. Liu, T. Canteenwala, et al. 2004. Effect of arm length on the aggregation structure of fullerene-based star ionomers. *J. Phys. Chem. B.* 108:14884–14888.

36. Cinelli, S., F. Spinozzi, R. Itri, S. Finet, F. Garsughi, et al. 2001. Structural characterization of the pH-denatured states of ferricytochrome-*c* by synchrotron small angle x-ray scattering. *Biophys. J.* 81:3522–3533.

37. Haubold, H. G., T. Vad, N. Waldofner, and H. Bonnemann. 2003. From Pt molecules to nanoparticles: in-situ anomalous SAXS studies. *J. Appl. Cryst.* 36:617–620.

38. Stuhrmann, H. B. 2007. Contrast variation in x-ray and neutron scattering. *J. Appl. Cryst.* 40:s23–s27.

39. Glatter, O., and O. Kratky, editors. 1982. Small Angle X-ray Scattering. Academic Press, New York.

40. Newville, M. 2001. IFEFFIT: interactive XAFS analysis and FEFF fitting. *J. Synchrotron Radiat.* 8:322–324.

41. Jiang, D. T., S. M. Heald, T. K. Sham, and M. J. Stillman. 1994. Structures of the cadmium, mercury, and zinc thiolate clusters in metallothionein: XAFS study of Zn_7-MT, Cd_7-MT, Hg_7-MT, and HgI_8-MT formed from rabbit liver metallothionein 2. *J. Am. Chem. Soc.* 116:11004–11013.

42. Zabinsky, S. I., J. J. Rehr, A. Ankudinov, R. C. Albers, and M. J. Eller. 1995. Multiple-scattering calculations of x-ray-absorption spectra. *Phys. Rev. B.* 52:2995–3009.

43. Orthaber, D., A. Bergmann, and O. Glatter. 2000. AXS experiments on absolute scale with Kratky systems using water as a secondary standard. *J. Appl. Cryst.* 33:218–225.

44. Lichtenegger, H. C., H. Birkedal, D. M. Casa, J. O. Cross, S. M. Heald, et al. 2005. Distribution and role of trace transition metals in *Glycera* worm jaws studied with synchrotron microbeam techniques. *Chem. Mater.* 17:2927–2931.

45. http://www.ccdc.cam.ac.uk/.

46. Silberberg, M. S. 2006. Chemistry, 4th ed. McGraw-Hill, New York.